Efficient and durable ZnO core-shell structures for photocatalytic applications in aqueous media

A. Sáenz-Trevizo, P. Amézaga-Madrid, P. Pizá-Ruiz, W. Antúnez-Flores,

C. Ornelas-Gutiérrez, M. Miki-Yoshida

Abstract

Core-shell nanostructures were synthesized by aerosol assisted chemical vapor deposition method. A ZnO nanorod (ZNR) was the core material, while the shell coating was individually film of Ti, Cu-Zn or Fe oxide. The crystalline phases of the synthesized materials were identified as oxides in the form of wurtzite (ZnO), anatase (TiO2), tenorite (CuO) and hematite (Fe2O3). Only for samples prepared using single Ti and Fe sources, amorphous shells were detected. The photocatalytic performance of all samples was tested by the discoloration of methylene blue. Findings confirmed that bare ZnO nanorods and commercial photocatalyst (Degussa P25) are comparable photocatalysts since 99% of dye discoloration was achieved in 60 min. Additionally, discoloration tests performed with the core-shell nanostructures revealed that the ZNR/TiO_x and ZNR/CuO-ZnO samples exhibited more than 93% of discoloration in 60 min. Nevertheless, with samples involving ZNR/Fe2O3 and ZNR/FeO_x/TiO2/Fe2O3, a maximum of 33% of dye discoloration was measured. Microstructural changes of the samples before and after the photo- catalysis essays were examined. Results showed that the bare ZnO and CuO-ZnO coated nanorods dis- solved in the aqueous medium. Conversely, the integrity of the ZnO core was evidenced through the morphological and structural analysis, when single TiO_x and multiple FeO_x and Fe2O3 layers, were

employed. Furthermore, quantitative measurement of Zn solubility was performed in selected samples to confirm dissolution inhibition. Noteworthy, outcomes suggest that the functionality of ZnO when applied in aqueous systems could be assured solely with the developed ZNR/TiO_x material.

Introduction

The fabrication of nanostructures comprising several coupled oxides has emerged as an effective alternative to obtain improved materials suitable for different applications; such applications include: gas sensors [1], hydrogen generators [2, 3], photocatalysts [4–16], solar cells [17] and UV photo-detectors [18]. For the same purposes and as a result of a higher proportion of surface to volume atoms available, one-dimensional (1D) structures have proved to be more appropriate materials [1, 3, 8–25]. From feasible semiconductors, ZnO represents a versatile material not only because its remarkable chemical and physical properties, but also for all of its technological applications [1–25]. As a photocatalyst, applied for wastewater treatment or for the destruction of organic pollutants, ZnO has showed high efficiencies and in some cases, even better results than those obtained within the utilization of conventional TiO2 photocatalysts [7, 11, 15, 17, 18, 23, 24], have been reported. However, ZnO dissolves when used in an aqueous medium [4, 19, 22–27]. For that reason, the development of protective layers to inhibit this effect while maintaining its photocatalytic property is a challenging task that still in progress. Several groups have already reported the functionality of ZnO based thin film heterostructures and core-shell materials by its effective combination with binary or ternary compounds, including: CuO [1, 6, 8, 16], CdS [2, 7, 10, 17], TiO2 [4, 9, 14, 18], SnO2 [5], In2O3 [5], Fe2O3 [11,

13], SrTiO2 [12], ZnS [3, 15], NiO [16] and WO3 [16]. Such combinations are primarily based on the proper band alignment and energy positions of the band edges [3, 13, 14, 17, 26, 27, 29–33]. Furthermore, ZnO has been also combined with polyaniline (PANI) and carbon materials (fullerene, nanotubes and graphene) [24, 25] in order to improve and preserve its property. Results showed that the previous composites exhibited an increase in the photo- catalytic activity and in some cases even the inhibition of the dissolution of ZnO was established. The later, derived from the progress of the photocatalytic property after multiple tests [4, 15, 18, 24, 25].

In agreement with preceding reports, the use of ZnO nanorod heterostructures coupled with different semiconductors, is an alternative approach to produce durable and efficient materials for photocatalytic applications. In consequence, this work focuses on the development of core-shell structures using ZnO nanorods (ZNR) as core materials and, binary metal oxides, such as TiO_x, CuO-ZnO, and Fe2O3 as shell layers. The ZNR were deposited onto TiO2 coated borosilicate substrates. All samples were prepared via aerosol assisted chemical vapor deposition (AACVD) technique. The morphology, crystalline structure, optical properties and photocatalytic performance were analyzed for the different coreshell nanostructures. The photocatalytic performance was tested through the discoloration of methylene blue (MB) in aqueous solution. Bare ZnO nanorods were used to compare the photocatalytic property of the synthesized nanostructures against a commercial powdered photocatalyst of TiO2 (Degussa P25) using different experimental configurations. The microstructure of the core-shell nanorods was analyzed before and after the photocatalytic test in order to evaluate its final condition and to determine the reusability of the coated and uncoated

ZnO nanorods. To our knowledge, there are no articles on the subject presenting morphological evidence of the samples after the photocatalytic test, in order to establish the microstructural affectations and to predict the durability of the photocatalyst. Additionally, quantitative measurement of Zn solubility was performed in ZNR and ZNR/ TiO_x samples to determine the dissolution inhibition capacity of the TiO_x shell.

Materials and methods

-Synthesis

Synthetized materials consisted of two, three or five layers of metal oxides grown onto borosilicate glass substrates (BGS) with dimensions of 2.5 cm x 2.5 cm. All materials were deposited using the aerosol assisted CVD technique. Bare samples comprising ZnO nanorods grown onto TiO2 coated BGS were obtained following the synthesis conditions as reported by Sáenz-Trevizo et al. [34]; this sample was used as a reference and it was designated as Z structure. Layered materials with core-shell configurations were formed by depositing a thin film (shell) of TiO_x, FeO_x or a composite of ZnO-CuO onto previously synthesized Z (core) samples; structures were named according to the outer oxide layer as T (for TiOx or TiO2), F (for FeOx or Fe2O3) and C (for CuO), respectively. Additionally, a shell structure comprising multiple layers was obtained by growing alternately FeO_x, TiO2 and Fe2O3 onto a Z structure; the sample was denoted as FTF material. The precursor type, its concentration, solvents, velocities, temperatures and carrier gas fluxes were optimized according to each synthetized layer. Further details of other synthesis conditions can be surveyed elsewhere [6, 34]. Table 1 summarizes the main deposition parameters employed within this work.

Table 1
Synthesis parameters employed for the development of the core-shell materials.

	Chemical composition	Precursor salt	Concentration (mmol dm^{-3})	Solvent	Deposition temperature (K)	Nozzle scan velocity (10^{-3} cm s^{-1})	Carrier air flux (dm^3 min^{-1})
Buffer layer	TiO_2	Titanium (IV) oxyacetylacetonate (90%)	50 ± 1	Methanol (99.8%)	673 ± 1	6.6 ± 0.1	5.00 ± 0.05
Core layer	ZnO	Zinc Chloride (97%)	100 ± 1	Deionized water	723 ± 1	3.3 ± 0.1	5.00 ± 0.05
Shell layer	TiO_2 or TiO_x	Titanium (IV) oxyacetylacetonate (90%)	50 ± 1	Methanol (99.8%)	673 ± 1	6.6 ± 0.1	10.0 ± 0.1
	CuO-ZnO	Copper (II) nitrate hemi-pentahydrate (99.99%) and zinc acetate (99.99%)	60 ± 1 for Cu 40 ± 1 for Zn	Methanol (99.8%)	673 ± 1	6.6 ± 0.1	5.00 ± 0.05
	Fe_2O_3 or FeO_x	Iron acetylacetonate (99%)	100 ± 1	Methanol (99.8%)	673 ± 1	10 ± 0.1	5.00 ± 0.05

-Microstructure and optical properties

Grazing incidence x-ray diffraction (GIXRD) patterns were acquired to determine the crystalline phases present on the synthesized structures. A Panalytical X-Pert system working with a Cu Kα radiation (λ¼ 0.1542 nm) operated at 40 keV and 30 mA was used for this purpose. Experimental parameters for the analysis were set as follow: the 2θ angle was varied between 20° and 80° at 0.05° of step and 2.75 s of step size time, having a grazing incidence angle fixed at 0.5°. Surface morphology was studied by field emission scanning electron microscopy (SEM) in a JEOL JSM7401F microscope. In addition, microstructural analysis of individual bare ZnO nanorods and core-shell structures, was performed by high-resolution scanning transmission electron microscopy (HR-STEM), which was accomplished with a JEOL JEM2200FSþCs high resolution microscope, equipped with a spherical aberration corrector in the condenser lens and operated at an accelerating voltage of 200 kV. For HR-STEM observations, nanorods were scratched from each sample and placed directly onto holey-carbon coated TEM grids. Energy dispersive x-ray spectroscopy (EDXS) in linescan mode was performed with an Oxford Inca x-sight detector attached to the TEM. Morphology and microstructure of the samples were studied before and after the photocatalytic activity

essays. Absorptance spectrum of the prepared samples was determined from total reflectance and transmittance measurements in the 300–2500 nm interval, using a UV–vis-NIR CARY 5000 spectrophotometer with a DRA2500 integrating sphere accessory.

-Photocatalytic activity

The photocatalytic activity of the samples was established through the discoloration of 1 cm3 of a solution of MB. Probe solution was prepared in deionized water at an initial concentration of 10-5 mol dm-3. During the test, the probe solution was contained inside a Teflon ring reactor of 2.1 cm diameter and 0.43 cm height. For the protection of the MB solution during the tests, the reactor was covered with a fused quartz cover. In order to promote fresh solution circulation over the photocatalyst surface, a small eccentric mass attached to a DC motor rotating at 2582 40 rpm was placed under samples stage. Initial photocatalytic activity essays were presented with and without the incorporation of the agitation system to validate its application. Comparative tests using a sample of bare ZnO nanorods (Z) and Degussa P25 (TiO2) as standard, were performed in order to verify the functionality of the core materials. The mass of P25 was set equal to the estimated mass of the total volume of ZnO nanorods inside the area of the Teflon ring. To partially immobilize the mass of P25, the powder was dispersed in methanol and then placed inside a Teflon ring that was previously attached to a clean BGS substrate. The methanol dispersion was dried at ambient conditions. Samples Z and P25 were exposed for 5, 15, 30 and 60 min under a black light blue bulb of 15 W (F15T8BLB) with wavelength emissions in the interval of 310 to 440 nm, and total irradiance of 1.8 mW cm-2. Further photocatalysis tests were performed using a visible light source: a commercial 15 W fluorescent lamp (F15T8D)

with wavelengths active in the interval of 350–750 nm and total irradiance of 3.1 mW cm-2. Fig. 1 exhibits the qualitative irradiance spectra of both light sources: the F15T8BLB black light blue bulb and the F15T8D fluorescent lamp, measured with a Thorlabs CCS200 compact spectrophotometer using a multimode optic fiber in the 200–1000 nm interval.

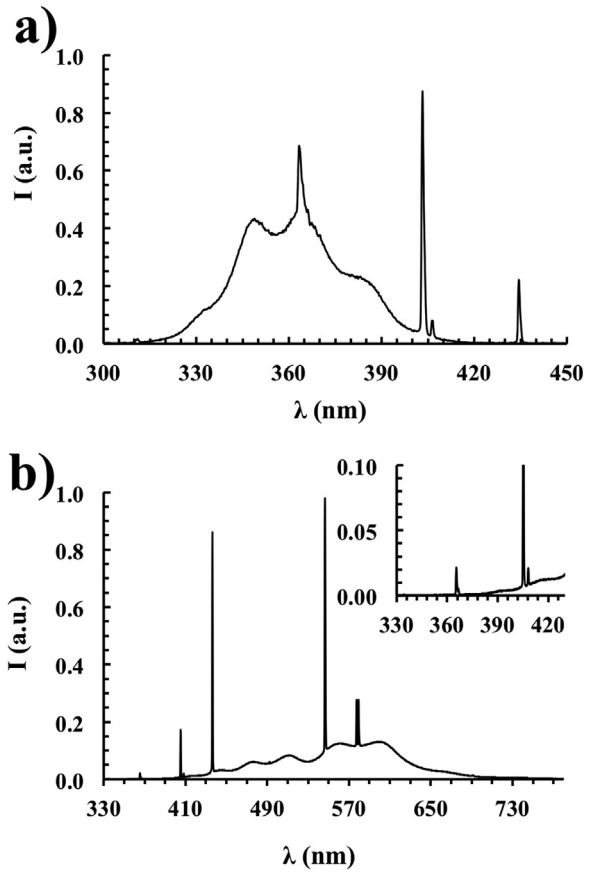

Fig. 1. Qualitative irradiance spectra of the light sources used in the photocatalytic tests a) F15T8BLB black light blue bulb; b) F15T8D fluorescent lamp.

Later on, the photocatalytic activity of the core-shell structures T, C, F and FTF, was evaluated using 1 cm3 of the MB solution at the same initial concentration. The

tests were carried out for periods of 60 min. Samples were irradiated employing the F15T8BLB bulb. The absorbance spectrum from all MB solutions that were in contact with the nanostructured materials and that were exposed to the light source, was measured in the 200–800 nm range in a UV–vis-NIR CARY 5000 spectrophotometer using a quartz cuvette holder. The MB absorbance peak located at 664 nm was correlated to dye concentration and was monitored as an indicator of photocatalytic efficiency.

-Quantification of Zn dissolution

In order to determine the solubility and durability of the ZnO nanorods, selected samples were immersed in 100 cm3 of distilled water. Samples were kept in dark at room temperature for a period of 24 h. Then, the quantification of dissolved Zn2þ was determined using an inductively coupled plasma-optical emission spectrometer (ICP) iCAP 600 Thermo Scientific.

Results and discussion

-Crystalline structure and microstructure

Grazing incidence X-ray diffraction patterns obtained from the developed structures appear in Fig. 2(a)–(d). The figure shows that all samples were polycrystalline and that in all cases, most of the peaks indicated the existence of ZnO as hexagonal wurtzite and TiO2 as tetragonal anatase (see Fig. 2(a)), consistent with the presence of ZnO nanorods and the TiO2 buffer layer in the nanostructure that was employed as core material (sample Z). For sample T (Fig. 2(b)), no modification of the crystalline components seen in sample Z was observed, neither was the formation of extra phases detected. For sample C (Fig. 2(c)) the upper layer containing CuO was

barely identified by the peaks at about 32.5°, 38° and 46.2°. For the case of sample F (not shown), no indication of Iron oxides was discerned, consistent with an amorphous phase, as reported previously [34]. However, for sample FTF in Fig. 2(d), two small peaks measured at about 24.1° and 33.2° indicated the existence of Fe2O3 as hematite. No peak position displacements or extra phases were detected within the analysis. Information suggests that no mixture between materials occurred. Identified ZnO, TiO2, CuO and Fe2O3 phases were in good agreement with PDF cards and 01-075-1533 [35], 00-021-1272 [36], 00-041-0254 [37] and 01-084-0308 [38], respectively.

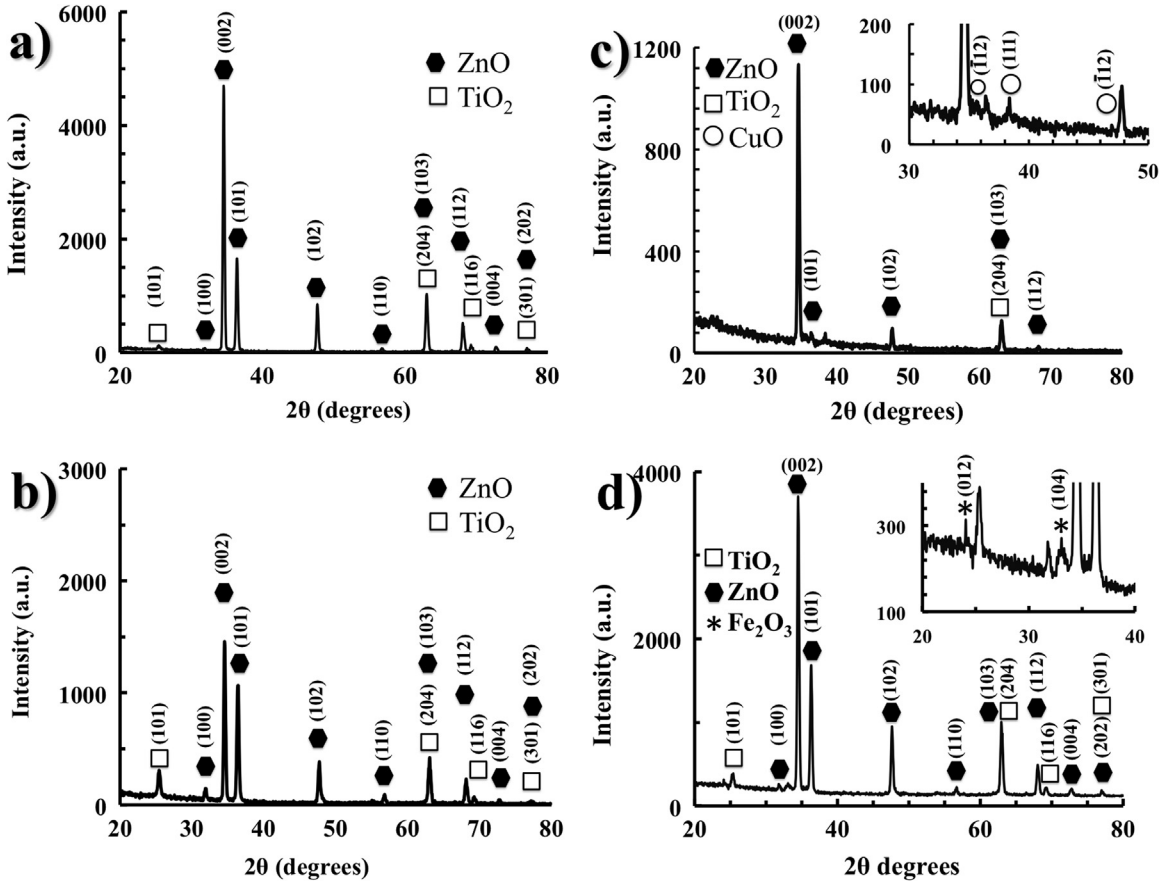

Fig. 2. GIXRD patterns showing the crystalline phases in bare ZnO nanorod and core-shell samples: a) bare ZnO nanorod, sample Z, b) TiO_x shell, sample T, c) CuO-ZnO shell, sample C and d) multilayered FeO_x-TiO_2-Fe_2O_3 shell, sample FTF. Results show the crystalline components of the synthesized structures.

Secondary electron SEM micrographs of the developed nanostructures are shown in Fig. 3. All samples displayed a uniform and dense evident layer of ZnO nanorods that appear as polyhedral columns; most of them having six defined planar facets. Structures emerged mostly ordered in the normal axis of the substrate. Fig. 3 (a) shows the morphology of the bare ZnO nanorods in sample Z evidencing the typical columnar morphology. Besides, there was no indication of pores, cracks or surface defects on the facets of the nanorods. Fig. 3(b) for sample T showed similar nanorods as those seen in sample Z and no clear evidence of the formation of the TiOx shell layer was perceptible. In contrast to previous structures, samples C and FTF shown in Fig. 3(c) and (d), respectively, exhibited ZnO nanorods with granular rough facets. The observed irregular finish was attributed to the deposit of an outer layer of CuO-ZnO and Fe2O3 in each case, revealing the development of a shell coating. As for sample FTF, surface morphology of sample F (not shown) exhibited nanorods with an irregular and granular finish.

Average nanorod length and width (distance between opposed facets) were determined as 1.570.2 μm and 3507180 nm, respectively. Previous estimations were made employing measure- ments from individual nanorods on several SEM micrographs from sample Z. Moreover, by considering these average dimensions, the specific surface area of the nanorods was estimated as 3.371.7 m2 g-1, a value that is at least one order of magnitude higher than the specific surface area of a flat ZnO film with a thickness equal to the length of the nanorod.

Further morphological and crystallographic observations were accomplished by HR-STEM in order to confirm the development of core-shell structures. Micrographs obtained from individual nanorods of samples T, C, F and FTF appear in Fig. 4. Figures are accompanied by insets achieved in bright field or Z contrast. All images revealed the formation of columnar structures as seen in SEM analysis, which were covered by uniform, continuous and homogeneous thin layers of material. For sample T in Fig. 4(a) a smooth, uniform and amorphous shell of TiOx with a thickness of around 1674 nm was noticed. Sample C in Fig. 4(b), exhibited a shell coating made of irregular nanoparticles of CuO and ZnO with sizes of about 2575 nm covering the surface of the ZnO nanorods. The crystalline phases of the shell particulates were confirmed by the measurements of the lattice fringes that were visible within this micrograph and whose dimensions were in accordance with the PDF cards of the previously identified oxides in Section 3.1. The development of a composite coating of ZnO-CuO was in agreement with the report of Sáenz-Trevizo et al. [6]. It is convenient to mention that the continuity of the CuO-ZnO layer was damaged during the preparation of the sample. For sample F in Fig. 4(c) an amorphous layer of material having a thickness of 1172 nm was detected. In consequence of the observed amorphous character of the shells in samples T and F, the identification of Ti and Fe oxides by GIXRD was not possible. Sample FTF in Fig. 4(d) evidenced a uniform three-layered shell structure grown onto the nanorods. The total thickness of the shell was about 2872 nm. For this sample, the Fe layer adjacent to the ZnO nanorod was also amorphous but the other consecutive TiO2 and Fe2O3 shells were polycrystalline. Each individual layer presented a thickness of about 872 nm. For all structures, the contrast caused by the differences in

composition of the deposited oxides was clearly observed. No combination or mixture of phases was detected be- tween the ZnO nanorod core and the other oxide shells or in between the different layers that comprised the multilayered shell. Moreover, as no difference in synthesis conditions or precursors took place for the formation of the single and multilayered core- shell structures, it was assumed that the amorphous Ti and Fe shells in T and F structures comprised the same crystalline phases seen in sample FTF, this being TiO2 and Fe2O3, respectively. Further information by EDXS, obtained in linescan mode from sample F, confirmed the existence of Fe2O3 according to the distribution of elements on the analyzed layer. Results from the analysis appear in Fig. 5.

-Optical properties

Absorptance spectrum of all samples as a function of photon energy was calculated from total reflectance and total transmittance measurements [34]. The corresponding spectra shown in Fig. 6 revealed that all materials presented optical absorption in the visible or UV region (1.6–4 eV). Some nanostructures also displayed a sharp absorption edge that matches closely to the optical band gap energy value of ZnO at around 3.2 eV [12, 16, 30, 32]. Moreover, great differences perceptible as a broader absorption band in the VIS region were detected on samples with a Cu or Fe oxide shell, which was an expected effect due to the lower band gap energy of these oxides. Accordingly, for sample C the absorption region extended at around 1.6 eV, associated to the presence of CuO (1.7 eV [30]) that was identified in Section 3.1. Similarly, for samples F and FTF, the absorption region that extended at about 2.1 eV was associated to the existence of Fe2O3 hematite, which has a lower band gap (2.2

eV [13, 30, 32, 39]). These predictable attributes motivated the application of the Cu and Fe oxides as a more efficient UV–vis light nanostructured photocatalyst. Further details about the estimation of the optical band gap of the sample of ZnO nanorods will be discuss in another paper.

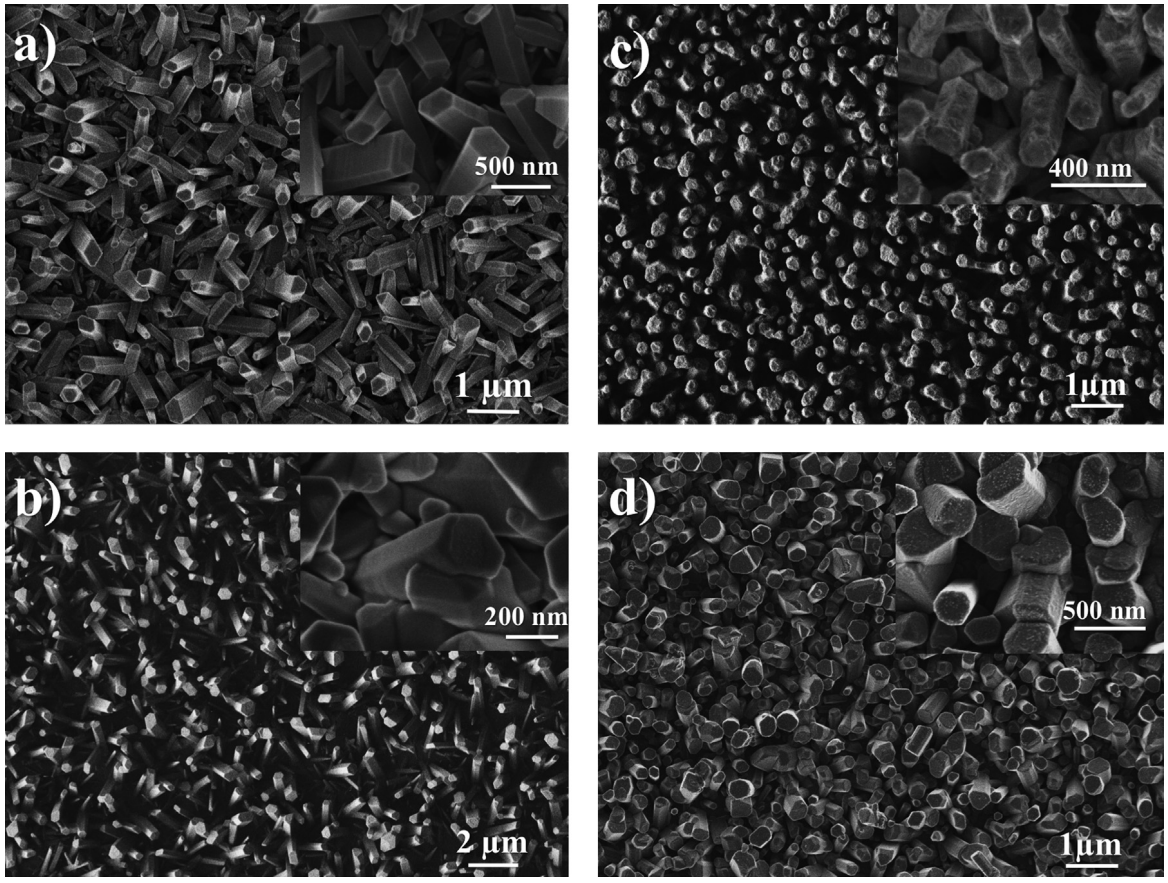

Fig. 3. Secondary electron SEM micrographs of: a) bare ZnO nanorods, sample Z; b) sample T, with TiO_x covered ZnO nanorods, c) sample C, CuO-ZnO covered ZnO nanorods and d) sample FTF, FeO_x-TiO_2-Fe_2O_3 covered ZnO nanorods. Images display the morphological differences developed when coating the ZnO nanorods.

-Photocatalytic activity

--Comparison of the photocatalytic activity of ZnO and P25 (TiO_2)

The photocatalytic activity of ZnO nanorods in sample Z was compared with a commercial standard of TiO2 (Degussa P25). Despite that the use of materials with discordant attributes (P25 powder and ZnO nanorods) to accurately set differences among photocatalyst is not fully recommended, the current analysis could serve to approach a validation about the functionality of the developed 1D nanostructures. For this purpose, the average dimensions of the nanorods in sample Z (1.570.2 mm in height and 350 nm 7180 nm of diameter) served to compute the volume and mass of ZnO in the sample (1.25 mg). Thus, the mass of P25 employed during the experiments matched the mass of the estimated ZnO inside the probe reactor.

Since the standard P25 is found in powder form, two experimental set-ups were first analyzed in order to establish optimal test conditions with regards to the stimulation of proper solution – photocatalyst contact. Initial tests were performed first without the incorporation of the agitation system developed. Both materials were in contact with 1 cm3 of the probe solution and were exposed under the black light blue bulb for periods of 60 min. Results were compared with experiments performed with the inclusion of the oscillating motor exposed under identical test parameters. The resulting reduction of the concentration of the dye achieved by each material appears summarized in Table 2. The corresponding UV–vis spectra that show the gradual variations in the absorbance of the probe solution after the discoloration tests appear in the supplementary Fig. S1. Findings revealed that similar and efficient results (from 77% and up to 99%) were obtained with both photocatalysts when used without and with agitation. Differences in the photocatalytic activity measured without the agitation system could be attributed to the contrast in particle size and shape between materials, which is linked to the amount

of photocatalyst and solution that come in contact. Morphological discrepancies could also lead to more effective light absorption or light loss due to scattering. Results also showed that, as expected, with the incorporation of the agitation device, the photocatalytic property of the samples increased. However, more favorable outcomes were noted for sample Z, whose photocatalytic activity augmented 22%. The previous observation suggests a reduction of time because of the continuous stirring, which guarantees a better solution – photocatalyst contact. According to previous results, the incorporation of the agitation system was established for all of the following tests.

Samples Z and P25 were employed for a complementary study in which the discoloration of the dye was evaluated as a function of time. Results from the essays appear summarized in Table 3. The UV–vis spectra of the probe solutions after the tests appear in the supplementary Fig. S2. It is clear from Table 3 that both samples exhibited a proportional increase in the discoloration of the dye over the established periods of time. Also, the materials exhibited favorable results after only 5 min of irradiation, suggesting an almost immediate response to the light source. On the other hand, a decrease in the photocatalytic activity of P25 during the consecutive experiments of 60 min was also observed. The effect was associated with the loss of powder after every run, when the exposed solution was collected for its respective spectroscopic measurement. The later observation confirmed one of the concerns about the application of photocatalysts in powder form in a liquid media, as it often requires the incorporation of additional stages for the recovery of the photocatalysts.

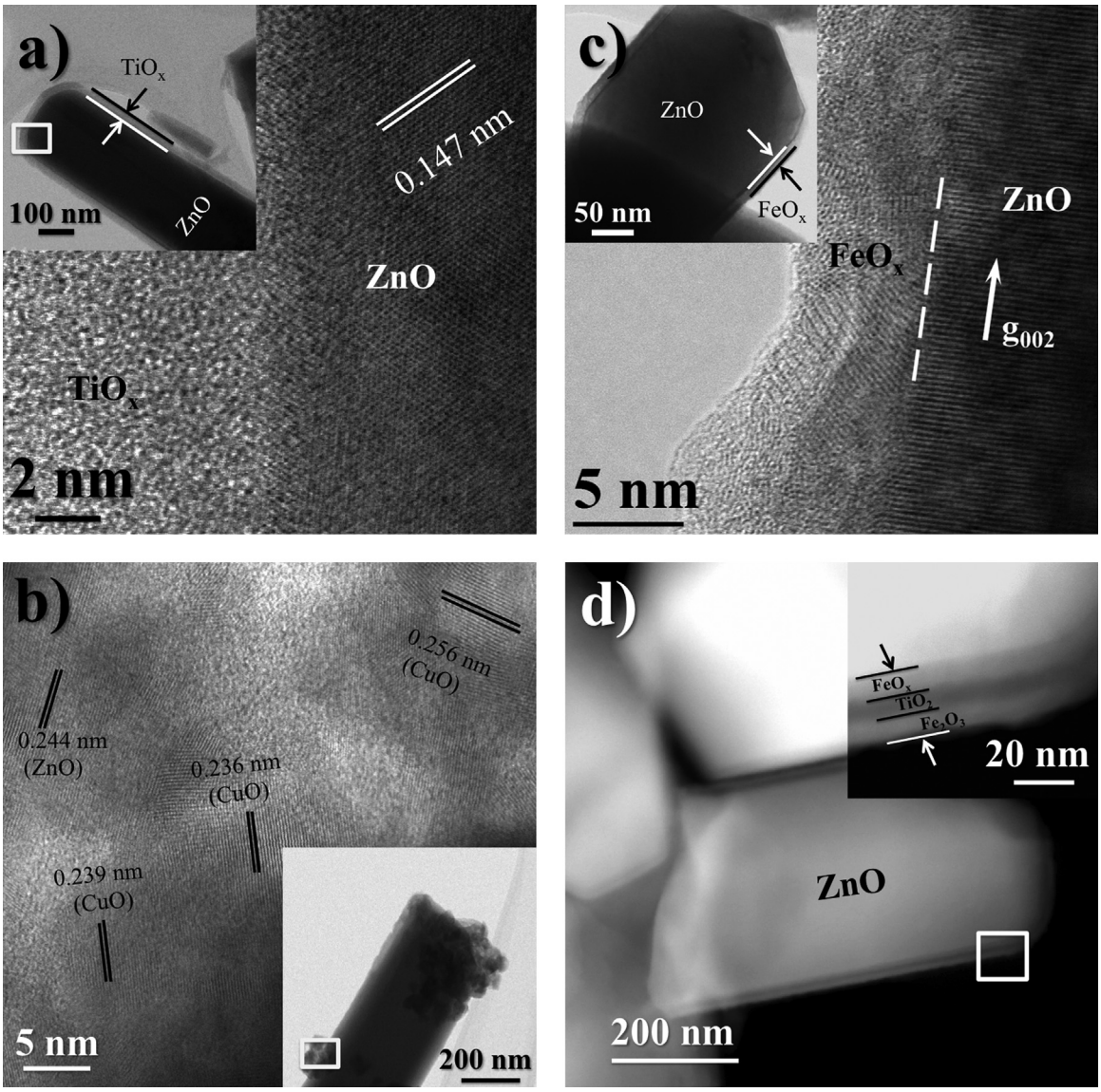

Fig. 4. Micrographs by HR-STEM of samples: a) T, b) C, c) F and d) FTF. Images reveal the nature of the developed core-shell structures.

Further photocatalysis tests were performed employing a visible lamp in order to evaluate the photocatalytic property of the materials in the presence of a commercial light source (F15T8D lamp). Outcomes from the 60 min runs appear summarized in Table 4. The UV–vis spectra of some of the various probe solutions collected after the

essays appear in the supplementary Fig. S3. Results show that both materials exhibited efficient results when exposed to the F15T8D lamp and in fact, these outcomes were similar to those results observed with the employment of the F15T8BLB bulb under the same conditions. These findings could be associated with the effective absorption of the energetically useful photons (from the UV region) arriving at the surface of the photocatalysts. As noted in Fig. 1, both light sources had emissions able to excite the ZnO and TiO2 in the samples. However, the visible light source has narrower emission spectra in the UV region if compared to the black light blue bulb. The efficient outcomes indicated that commercial devices could be applied conveniently for the treatment of pollutants. Indeed, additional photocatalytic tests with monochromatic UV and visible light are currently in progress, with the aim to explain these favorable outcomes and to explore the molecular phenomena that takes place when the dye is exposed under different wavelengths.

Overall outcomes presented so far confirmed that P25 as well as ZnO in the form of nanorods are functional and efficient photocatalysts. Advantages of P25 over ZnO were mostly attributed to its higher specific surface area (about 50 m2 g-1 against 3.371.7 m2 g-1) and also to its dissolution resistance as stated before by Neppolian et al. [26]. However, P25 requires additional removal stages once it has been used in aqueous media, as mentioned earlier; this phenomena is linked with the immobilization problems. By using a photocatalyst supported onto substrates, this situation was overcome. Noteworthy, a clean BGS substrate attached to a Teflon ring was used as a reference, in order to dismiss photolysis of the dye when exposed to the light source and when used without photocatalyst. Results showed that within the various runs, a

reduction of the concentration of the dye with a maximum of 1073% was detected using the F15T8BLB lamp. Therefore, photolysis was not considered as the responsible mechanism for the considerable discoloration of the dye observed during the several runs.

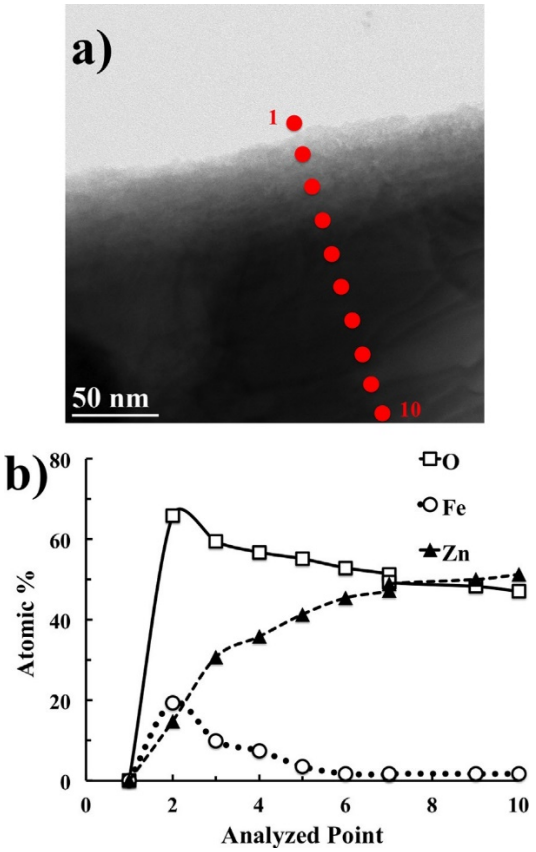

Fig. 5. a) Bright field STEM micrograph of sample F, showing the zone of the EDXS linescan; b) Fe, Zn and O composition in at% for each marked point along the linescan shown in a).

--Photocatalytic activity of core-shell materials

In search of more efficient and durable materials, the evaluation of the photocatalytic property of the developed core-shell structures synthesized in this work was also analyzed. Table 5 displays the average discoloration values of MB achieved

after several runs of 60 min using the synthesized T, C, F and FTF samples. The corresponding UV–vis spectra of some of the probe solutions evaluated appear in the supplementary Fig. S4. For the current tests, sample Z was also used as a reference. According to Table 5, similar and effective photocatalytic performances were fulfilled by samples Z, T and C, since dye discoloration values of more than 93% and up to 99% were accomplished with these materials. Outcomes suggest that functional photocatalysts were developed with the incorporation of TiO_x and CuO oxides, as reported in references [4, 9, 14] for TiO2 and [6, 8] for CuO. Results for sample Z were in agreement with the analysis presented in Section 3.3.1.

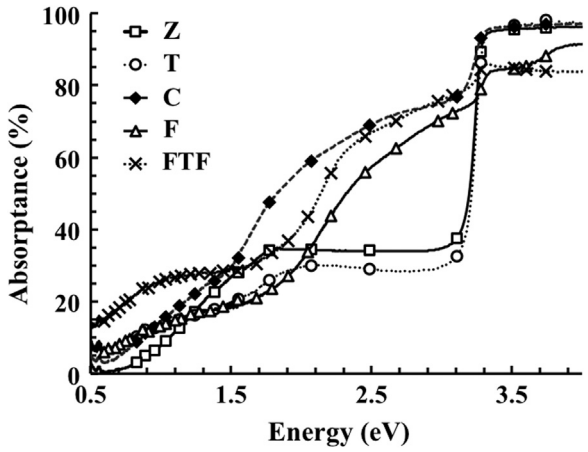

Fig. 6. Absorptance spectra of the ZnO nanorod (core) – metal oxide (shell) ma- terials compared with a sample of bare ZnO nanorods (Z).

Table 2
Discoloration of MB fulfilled with and without the agitation of the probe solution.

Sample		Z	P25
Dye discoloration (%)	**Test without agitation**	77.0 ± 0.8	89.0 ± 0.4
	Test with agitation	99.0 ± 0.9	99.00 ± 0.02

Table 3
Discoloration of MB achieved as a function of exposure time.

Sample		Z	P25
Dye discoloration (%)	**5 min**	42.5 ± 0.1	52.1 ± 0.3
	15 min	71.4 ± 0.1	61.6 ± 0.2
	30 min	93.8 ± 2.3	94.5 ± 0.4
	60 min	99.2 ± 0.1	92.0 ± 0.2

Table 4
Dye discoloration fulfilled with the employment of commercially available visible (F15T8D) lamp.

Sample	Z	P25
Dye discoloration (%)	92.2 ± 2.5	99.6 ± 0.2

Table 5
Average values of MB discoloration by the bare and core-shell nanorods.

Sample	Z	T	C	F	FTF
Dye discoloration (%)	99.2 ± 0.1	97 ± 2	93 ± 1	33 ± 6	10 ± 4

Table 6
MB discoloration by the bare and core-shell nanorods using CH_3OH as scavenger in the probe solution.

Sample	Z	F	FTF
Dye discoloration in presence of methanol (%)	23 ± 1	22.0 ± 0.1	5.0 ± 0.1
Reduction of photoactivity (%)	76	33	50

Recalling absorption spectra in Fig. 6, it was expected that all structures could achieve optimum dye removal values in the UV region at above 3.1 eV, which is the active wavelength range provided by the UV-A light source employed (F15T8BLB lamp with emissions from 310 to 440 nm). Nevertheless, none of the samples that incorporated Fe oxides presented efficient photocatalytic response (maximum of MB discoloration of 33%). Different and successful results from those obtained herein with the evaluation of samples F and FTF (both comprising shells of Fe2O3), were presented by Liu et al. [11] and Achouri et al. [13]. The first group argued that their synthesized ZnO/Fe2O3 photocatalyst presented higher photocatalytic efficiencies than the bare ZnO nanorods (up to 98% of MB discoloration in 60 min). The researchers attributed the effective outcomes of the core-shell structure to various phenomena (available surface area, broader absorption of light and the proper band alignment). However, it was not considered that the hollowed sample presented two different facets exposed: the first one corresponding to the inner surface that was formed because of the dissolution of the nanorod core during the synthesis of the shell, and the second one, being the outer surface of Fe2O3 that was grown onto the primary nanorod; both forming the reported nanotube. Consequently, the two different and active available surfaces in the same nanostructure could lead to an increment of the photocatalytic response observed within the ZnO/ Fe2O3 sample. Besides, the size or thickness of the shell was not presented, which is a critical factor for the photocatalytic effectiveness of the Fe2O3 materials. The later since this particular oxide does exhibit a short diffusion path length (about 2–4 nm) for the migration of the generated electrons (e-) and holes (hþ) towards the surface [32,39]. In fact, Achouri et al. [13] presented another report

exhibiting the efficient photocatalytic activity of a ZnO/Fe2O3 core-shell structure, in where the average diameter of the particulates that comprised the shell was determined of about 3 nm. Therefore, this magnitude falls within the range of the re- ported effective diffusion length of the pairs (e- and h^{p}) [39] and, supports then the functionality of their sample. In accordance with foregoing information, the thickness of the Fe2O3 layers could be the main reason for the deficient photocatalytic behavior of the prepared F and FTF samples, which only exhibited 33% and 10% of MB discoloration, respectively. Differences in efficiency between the photocatalyst presented by Achouri et al. [13] and the samples presented in this report could be also attained due to morphological discrepancies. This being because the Fe2O3 layer in their report consisted of spherical particulates instead of continuous thin films, as depicted herein. Additional determining factors such as carrier mobility among semiconductors or the extension of the interface region were not considered, but they can exert influence on the photocatalytic performance of the heterostructures as mentioned recently by Li and Wu [32].

On the other hand and according to the optical properties of the materials presented in Section 3.2, all of the synthesized oxides in samples F and FTF are able to absorb photons from the light source (F15T8BLB) at the same time. However, because of their low band gap, the layers of FeOx or Fe2O3 reduce the amount of pho- tons that can be absorbed for the highest band gap materials (ZnO or TiOx). As a consequence and, because of the limitations of the Fe layers, not all of the arriving photons are useful in the photo- catalytic process.

Based on previous information, a possible mechanism for the interaction of ZnO/FeOx/TiO2/Fe2O3 in sample FTF and analogously for sample F, can be explained as follows:

The photogenerated e- and $h^{þ}$ on the ZnO nanorod transfer to the conduction and valence bands of the immediate shell of Fe2O3. Then, because of the limited diffusion length, only some pairs reach the surface (sample F) or the second shell of TiO2 (sample FTF). Besides, at this layer, an additional obstacle probably takes place in both samples. The later because the Fe shell is simultaneously generating e- and $h^{þ}$, giving rise to the existence of available sites where some of the initial e- and $h^{þ}$ can recombine, while the remaining ones can migrate up to the surface or to the consecutive oxide layer. This mechanism is also applicable for the second (TiO2) and third (Fe2O3) shells in sample FTF, resulting in the continuous reduction of the pairs that can migrate up to the surface.

As the photocatalytic activity of sample FTF was almost a third part of the photocatalytic activity of sample F, the above-mentioned phenomenon proved that a scarce portion of the generated e- and $h^{þ}$ arrived at the surface. This was because its trajectory was hindered in the first place due to the thickness of the shell layer (about 8 nm) and then, reduced during its migration among various photoactive semiconductors as a consequence of the simultaneous absorption of photons and generation of pairs. Mechanism for sample T will be discussed later in text.

Noteworthy, the lack of a crystalline characteristic in the shell layer (samples T and F) did not behave as a limiting factor for the photocatalytic performance of the synthesized nanostructures. In fact, the work of Cheng et al. [14] agrees on the

enhanced functionality of core-shell material that incorporates crystalline ZnO and amorphous TiO2, as presented herein in sample T.

On the other hand and since it is known that e- and $h^{þ}$ in the presence of water yield to the existence of strong oxidizing agents (such as OH• and O2•- radicals) that can degrade the MB molecules, an additional experimental test was set in order to reveal the nature of the oxidative species in the photocatalytic process. Thus, 0.123 mmol of CH3OH were added to the probe solution. Results from the test appear summarized in Table 6, whose photocatalytic activity was compared with the results obtained in Table 5. The corresponding UV–vis spectra of the probe solutions collected after the test appear in the supplementary Fig. S5. Out- comes in Table 6 show that the photocatalytic property of all the materials decreased. For sample Z, its activity was reduced at a great extent, going from 99% to 23% of dye discoloration (reduction of about 76%). For samples F and FTF, whose photocatalytic property was not effective, its activity was also reduced (reduction from 33% to 55%). Results suggest that in the case of bare ZnO nanorods in sample Z, holes behaved as the main oxidative species. The later, as it is known that CH3OH acts as hole scavenger [15, 39] and its inclusion in the probe solution affected considerably the photocatalytic performance of the sample. For samples with Fe oxides (F and FTF), findings suggest that holes, OH• radicals and probably other oxygen species are responsible for the photocatalytic performance of the materials. This, as the photocatalytic property was affected to a lesser extent. Moreover, the scarce reduction in the photocatalytic activity of these samples could serve to corroborate that only a few portions of holes reached

the surface and thus, supporting once again the information about the limited diffusion path length for the migration of pairs in Fe2O3.

-Dissolution inhibition of ZnO nanorod

Despite that similar photocatalytic activities were observed with samples Z and T in Sections 3.3.1 and 3.3.2, it is expected that the efficiency of sample Z will decrease as a consequence of ZnO dissolution. Therefore, additional microstructural observations were accomplished in order to evaluate the conditions of the samples after the photocatalysis tests. Micrographs of the core- shell nanostructures obtained by SEM after the tests, appear in Fig. 7. For sample Z in Fig. 7(a), an obvious decrease in facets and edge definition was observed. This occurred as the sharp and continuous polyhedral edges of the columnar bodies disappeared and thus, almost flat bars remained. Besides, there was no clear evidence of the modification of the length of the nanorods. For sample T in Fig. 7(b), the deterioration of the nanostructures after the experimental runs was not visibly noted. This, as the TiO_x covered nanorods appear almost unscathed. For sample C in Fig. 7 (c) small crumbs dangling over the nanorods emerged, indicating a clear reduction of the CuO-ZnO layer. However, insignificant shape changes in the hexagonal structure of the ZnO nanorods were noted. This information demonstrates that the CuO-ZnO shell was washed away as an indication of material dissolution. Perhaps because of the rapid dissolution of ZnO and CuO grains that adheres both crystalline phases of the shell layer. For sample FTF in Fig. 7(d) it is clearly shown that any surface damage was caused by MB solution, suggesting that the corresponding exposed layers could be suitable for ensuring the dissolution inhibition of ZnO in aqueous media. Nevertheless, the dye discoloration results were insufficient as

proved in Section 3.3.2. Same nanorods condition was observed in sample F. Additional micrographs for sample T and FTF obtained by HR-STEM and SEM using TEM grids containing individual nanorods, appear in Fig. 8. From the figure and for both samples, no apparent damage on the materials surface was noted. Also, the continuity of the upper layer was also preserved after the several essays. Observed irregularities may be caused when manipulating the samples during every run or due to the presence of traces from organic matter.

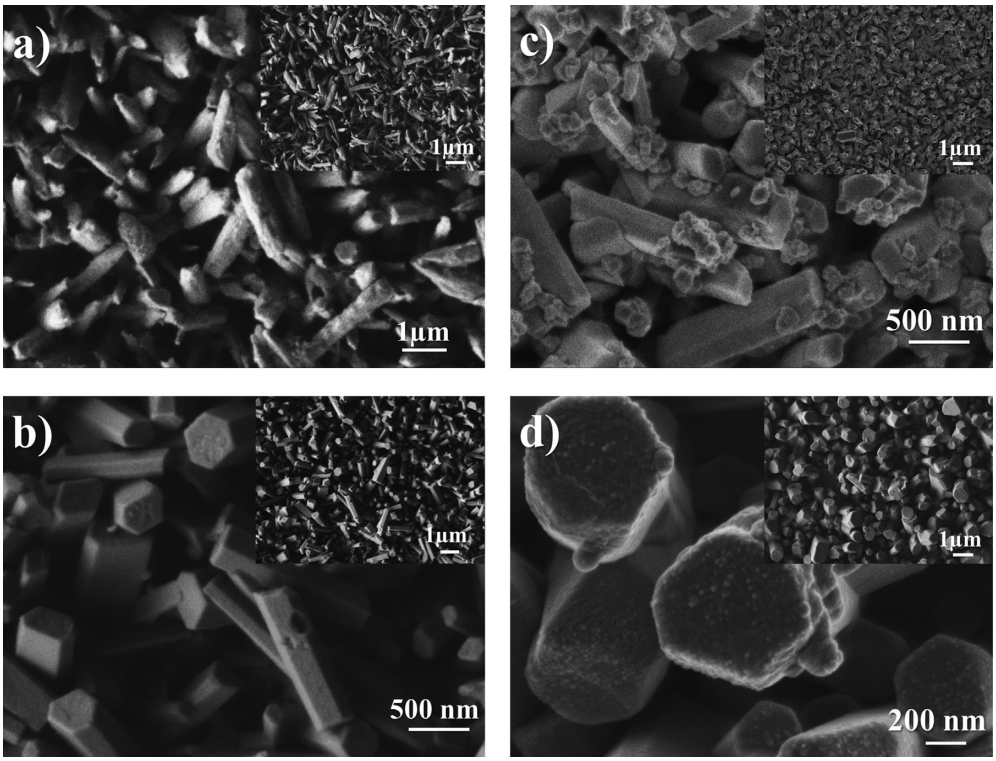

Fig. 7. Micrographs by SEM from samples: a) sample Z, b) sample T, c) sample C and d) sample FTF after the photocatalytic essays. Images display the morphological modifications of the nanostructures caused by the probe solution.

The dissolution of ZnO noticed in this work by means of the modification of the polyhedral edges of the nanorods, was expected as discussed earlier by Sapkal et al.

[4], Neppolian et al., [26], Bard [27], Franklin et al. [28], Chen and Wang [29] and Xu and Schoonen [30]. As a matter of fact, the deterioration of the edges fitted with the statements of Borm et al. [40], who related the shape and surface characteristics of the nanostructures with the rate of dissolution of the materials. Borm [40] argued that the concave or convex features of the nanoparticles play a significant role in the dissolution process and, suggested that dissolution occurs first at the convex faces of the particulates. Thus, it was expected that the erosion of the ZnO nanorods occurred preferably on the edges rather than at the faces. This information matched with the negligible modification of the length of the nanorods, as shown in Fig. 7. Furthermore, the efficient photocatalytic activity was preserved in samples Z and C because of the existence of a considerable amount of ZnO. Likewise, predictions about the durability of ZnO in the samples can be deduced from the studies of Franklin et al. [28], who found that the rate and limit of ZnO dissolution was of about 16 mg dm-3 (pH 7.6). This means that using the mass of ZnO (of 1.25 mg) and the volume of probe solution of 1 cm3, it can be estimated that samples Z and C will last for at least 78 experiments. This approximation could serve to predict the functionality of the photocatalyst when working under aqueous conditions.

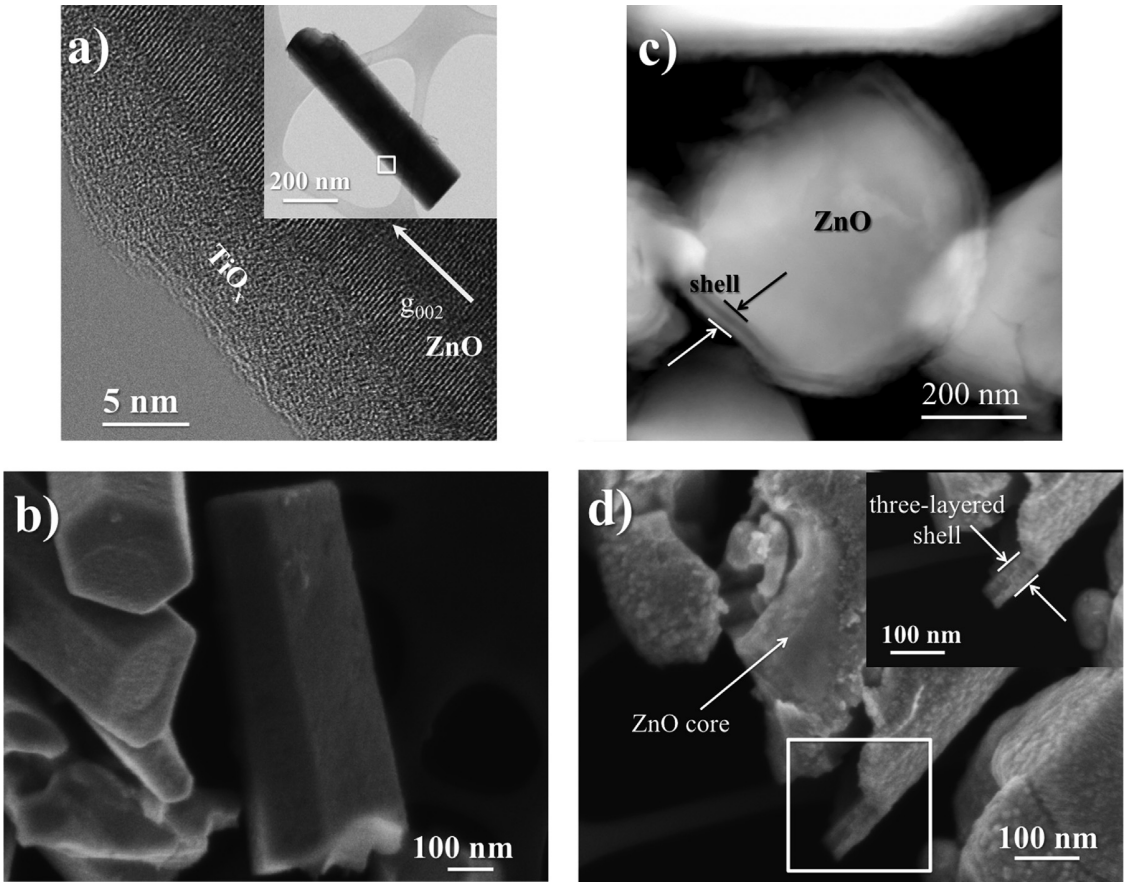

Fig. 8. a) Bright field and b) SEM micrographs of nanorods from sample T; c) Z contrast and SEM micrograph from nanorods in sample FTF. Images show the integrity of the core-shell structure.

In contrast to previous phenomena, the deterioration of TiO_x or FeO_x and Fe2O3 layers was not expected [32]. Observations on micrographs in Figs. 7 and 8 for these samples confirmed the later information. Outcomes revealed clear morphological evidence regarding the protective effect of the single and multiple TiO_x, TiO2, FeO_x or Fe2O3 shell coatings.

On the other hand, according to the band structure developed in sample T, the photogenerated e- in the conduction band of TiO_x could be transferred to the conduction band of ZnO, while the photogenerated $h^þ$ in the valence band of ZnO could be

transferred to the valence band of TiO_x. As a result, the availability of e- and $h^þ$ at the surface of the core-shell photocatalyst for the occurrence of redox reactions was preserved, explaining the effectiveness of the photocatalyst, as reported in other works [4, 14]. Concurrently, by having a TiO_x shell, the dissolution of ZnO attributed to the reaction of $h^þ$ with oxygen atoms at its surface (as it occurs with CdS [32]), it can be inhibited or reduced by the aforementioned mechanism. The latter as $h^þ$ are transferred to the upper layer and then, to the surface adsorbed water, dye or oxygen molecules, instead of remaining at the surface of ZnO, where they can consume this oxide. A comparable conclusion about the inhibition of ZnO dissolution was stated by Tu et al. [12], who developed a ZnO/SrTiO3 core-shell structure.

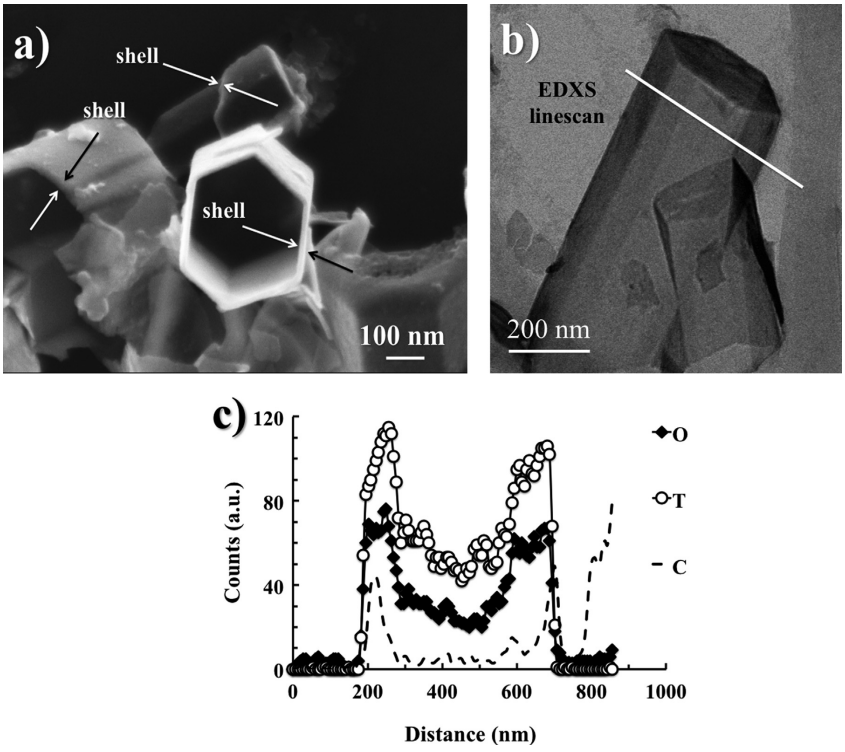

Fig. 9. a) SEM micrograph from nanorods etched in a solution of acetic acid; b) HR-STEM bright field micrograph from nanorods in acetic acid and c) its corresponding EDXS linescan analysis. Results show the preservation of the TiO_x shell.

Additionally, in order to prove that the layer of TiO_x could effectively reduce the dissolution of the ZnO core in the aqueous media, it was quantified the $Zn^{2þ}$ dissolved from selected samples. For this purpose, samples Z and T were immersed in deionized water for a period of 24 h. Only nanorods from sample T were selected for further analysis as the photocatalytic property of the material was assured by using this combination of oxides. Results measured by ICP showed that Ti was not detected in none of the volumes of water that were in contact with the nanostructures. However, in both cases it was determined the presence of $Zn^{2þ}$ dissolved in water: 0.18670.028 mg dm-3 for sample Z and 0.03770.024 mg dm-3 for sample T. Outcomes confirmed that, as expected, having a shell layer of TiO_x the amount of dissolved ZnO was reduced. Moreover, the detection of $Zn^{2þ}$ dissolved from sample T was mostly attributed to the existence of ZnO exposed at the edges of the sample and also, due to the presence of damaged nanorods. The former, because the coating did not covered entirely the bottom of the nanostructures. Thus, since some of the nanorods are interconnected at the bottom, the water could penetrate and react with the core of ZnO.

Furthermore, a simple etching process similar to that in [41] was carried out in diluted solutions of acetic and hydrochloric acid in order to confirm the protective effect of the TiO_x shell in an acidic aqueous media. The current experiment intended to emulate a severe corrosive environment [15]. For this purpose, drops of each acid were added until the pH of the solution was lowered to 1. Later, nanorods that were previously scratched from sample T were placed into the containers for 1 h. For morphological observations by SEM and HR-STEM, few drops from each container

were placed onto Si wafers and TEM grids. Fig. 9 displays the microstructural changes on TiO_x coated ZnO nanorods after the etching procedure.

Fig. 9(a) and (b) shows that in both cases the core of ZnO was removed and thus, only the shell material was left. Evidently, the remaining hollowed shell material preserved the primary hexagonal structure of the ZnO nanorods. Fig. 9(c) shows the results from an EDXS analysis in linescan mode that was performed to the remaining empty shell in Fig. 9(b) in order to corroborate the composition of the particulate. The analysis showed that only Ti and O formed the shell. Carbon residues were attributed to organic matter. Findings proved that the developed TiO_x shell coating was suitable for ZnO nanorod protection even under an acid medium. However, further dissolution tests, as a function of time, pH and illumination, are needed in order to define precise solubility limits in dark and upon exposure under a light source. This since it has been stated that dissolution of ZnO is shape, size and pH dependent [28, 40] and also accelerated in the presence of light [4, 15, 32].

Conclusions

Nanostructured core-shell materials consisting of superimposed oxide layers over ZnO nanorods were successfully prepared solely via the AACVD technique. Sample Z used as a core, had comparable photocatalytic activity than a commercial photocatalyst (P25). On the other hand, samples covered separately with TiO_x or CuO-ZnO layers, exhibited high (493%) photocatalytic activity for the discoloration of MB in solution, when irradiated with a UV-A light source during 60 min. Otherwise, morphological and microstructural evidence suggested that ZnO nanorod protection was achieved by individual application of a TiO_x, or single and multilayered Fe2O3 (FeO_x) shell. Inhibition

dissolution of ZnO was confirmed in the TiO_x covered sample by quantification of dissolved Zn in water. Overall outcomes showed that within the application of a TiO_x onto the ZnO nanorods, a durable and efficient photocatalyst was produced. However, in order to avoid rapid core dissolution, it has to be assured that no surface defects or uncoated edges get exposed. Then, these core-shell materials can be adopted for applications that involve aqueous systems.

Acknowledgments

The authors would like to thank to the following people: S. Miranda, P. Peregrino, A. Rubio, O. Solis, C. Leyva, K. Campos, E. Guerrero, A. Benavides and O. Esquivel for the technical assistance they provided during the undertaking of this work. The authors would also like to thank SEP-CONACYT (Project no. 242612) for their partial financial support.

Appendix A. Supporting information

Supplementary data associated with this article can be found in the online version at doi:10.1016/j.mssp.2016.01.018.

References

[1] J. Kim, W. Kim, K. Yong, J. Phys. Chem. C 116 (2012) 15682–15691. [2] X. Chen, S. Shen, L. Guo, S.S. Mao, Chem. Rev. 110 (2010) 6503–6570.

[3] Y. Liu, Y. Gu, X. Yan, Z. Kang, S. Lu, Y. Sun, Y. Zhang, Nano Res. 8 (2015) 2891–2900.

[4]

R.T. Sapkal, S.S. Shinde, T.R. Waghmode, S.P. Govindwar, K.Y. Rajpure, C. H. Bhosale, J. Photochem. Photobiol. B 110 (2012) 15–21.

[5] N. Talebian, M.R. Nilforoushan, Z. Salehi, Ceram. Int. 38 (2012) 4623–4630.

[6] A. Sáenz-Trevizo, P. Amézaga-Madrid, P. Pizá-Ruíz, O. Solís-Canto, C. Ornelas-Gutiérez, S.A. Pérez-García, M. Miki-Yoshida, J. Alloy. Compd. 615 (2014) S375–S381.

[7] W. Shouqiang, S. Zhongcai, L. Xudong, L. Ying, C. Linlin, H. Yan, J. Environ. Sci. 21 (2009) 991–996.

[8] Z. Liu, H. Bai, D.D. Sun, Int. J. Photoenergy 2012 (2012), ID804840.

[9] R. Wang, H. Tan, Z. Zhao, G. Zhang, L. Song, W. Dong, Z. Sun, J. Mater. Chem. A 2 (2014) 7313–7318.

[10] S. Khanchandani, S. Kundu, A. Patra, A.K. Ganguli, J. Phys. Chem. C 116 (2012) 23653–23662.

[11] Y. Liu, L. Sun, J. Wu, T. Fang, R. Cai, A. Wei, Mater. Sci. Eng. B 194 (2015) 9–13.

[12] Y.F. Tu, Q.M. Fu, X.J. Niu, J.P. Sang, Z.J. Tan, G. Zheng, X.W. Zou, Cryst. Res. Technol. 48 (2013) 138–144.

[13] F. Achouri, S. Corbel, A. Aboulaich, L. Balan, A. Ghrabi, M.B. Said, R. Schneider, J. Phys. Chem. Solids 75 (2014) 1081–1087.

[14] C. Cheng, A. Amini, C. Zhu, Z. Xu, H. Song, N. Wang, Sci. Rep. 4 (2013) 1–5.

[15] L. Yu, W. Chen, D. Li, J. Wang, Y. Shao, M. He, P. Wang, X. Zheng, Appl. Catal. B Environ. 164 (2015) 453–461.

[16] S.-M. Lam, J.-C. Sin, A.Z. Abdullah, A.R. Mohamed, Sep. Purif. Technol. 132 (2014) 378–387.

[17] T. Bora, H.H. Hyaw, J. Dutta, Electrochim. Acta 68 (2012) 141–145.

[18] S. Panigrahi, D. Basak, Nanoscale 3 (2011) 2336–2341.

[19] S. Baruah, M.A. Mahmood, M.T.Z. Myint, T. Bora, J. Dutta, Beilstein J. Nano-technol. 1 (2010) 14–20.

[20] A. Sapkota, A.J. Anceno, S. Baruah, O.V. Shipin, J. Dutta, Nanotechnology 22 (2011) 215703–215710.

[21] X. Li, J. Wang, J. Yang, J. Lang, S. Lü, M. Wei, X. Meng, C. Kou, X. Li, J. Alloy. Compd. 580 (2013) 205–210.

[22] B.R. Mehta, F.E. Kruis, Sol. Energy Mater. Sol. Cells 85 (2005) 107–113. [23] S. Xu, Z.L. Wang, Nano Res. 3 (2011) 676–684.

[24] H. Zhang, R. Zong, Y. Zhu, J. Phys. Chem. C 113 (2009) 4605–4611.

[25] C. Han, M.-Q. Yang, B. Wengab, Y.-J. Xu, Phys. Chem. Chem. Phys. 16 (2014) 16891–16903.

[26] B. Neppolian, S. Sakthivel, Banumathi Arabindoo, M. Palanichamy, V. Murugesa, J. Environ. Sci. Health A Toxic Hazard. Subst. Environ. Eng. 34 (1999) 1829–1838.

[27] A.J. Bard, M.S. Wrighton, J. Electrochem. Soc. 24 (1977) 1706–1710.

[28] N.M. Franklin, N.J. Rogers, S.C. Apte, G.E. Batley, G.E. Gadd, P.S. Casey, Environ. Sci. Technol. 41 (2007) 8484–8490.

[29] S. Chen, L.-W. Wang, Chem. Mater. 24 (2012) 3659–3666.

[30] Y. Xu, M.A.A. Schoonen, Am. Mineral. 85 (2000) 543–556.

[31] H. Zhu, T. Lian, Energy Environ. Sci. 5 (2012) 9406–9418. [32] J. Li, N. Wu, Catal. Sci. Technol. 5 (2015) 1360–1384.

[33] A.L. Linsebigler, G. Lu, J.T. Yates, Chem. Rev. 95 (1995) 735–758.

[34] A. Sáenz-Trevizo, P. Amézaga-Madrid, P. Pizá-Ruiz, W. Antúnez-Flores,

C. Ornelas-Gutiérrez, M. Miki-Yoshida, Mater. Charact. 105 (2015) 64–70. [35] PDF 01-075-1533, ICDD, 2010.

[36] PDF 00-021-1272, ICDD, 2010.

[37] PDF 00-041-0254, ICDD, 2010.

[38] PDF 01-084-0308, ICDD, 2010.

[39] Y. Huang, D. Ding, M. Zhu, W. Meng, Y. Huang, F. Geng, J. Li, J. Lin, C. Tang, Z. Lei, Z. Zhang, C. Zhi, Sci. Technol. Adv. Mater. 16 (2015) 014801–014813.

[40] P. Borm, F.C. Klaessig, T.D. Landry, B. Moudgil, J. Pauluhn, K. Thomas, R. Trottier, S. Wood, Toxicol. Sci. 90 (2006) 23–32.

[41] X. Huang, M. Wang, M.-C. Willinger, L. Shao, D.-S. Su, X.M. Meng, ACS Nano 6 (2012) 7333–7339.